



# Computation of a high Reynolds number jet and its radiated noise using large eddy simulation based on explicit filtering

Christophe Bogey <sup>\*</sup>, Christophe Bailly

*Laboratoire de Mécanique des Fluides et d'Acoustique UMR CNRS 5509, Centre Acoustique, Ecole Centrale de Lyon,  
36 avenue Guy de Collongue, 69134 Ecully, France*

Received 29 April 2004; received in revised form 13 December 2004; accepted 25 April 2005  
Available online 19 August 2005

---

## Abstract

An isothermal circular jet with a Mach number of  $M = 0.9$  and a Reynolds number of  $Re_D = 4 \times 10^5$  is computed by compressible large eddy simulation (LES). The LES is carried out using an explicit filtering to damp the scales discretized by less than four grid points without affecting the resolved large scales. The jet features are thus found not to appreciably depend on the filtering procedure. The flow development is also shown from simulations on different grids to be independent of the location of the grid boundaries. The flow and the sound field obtained directly by LES are compared to measurements of the literature. The acoustic radiation especially displays spectra and azimuthal correlation functions which behave according to the observation angle as expected for a high Reynolds number. Furthermore the two components of jet noise usually associated to large structures and to fine-scale turbulence, respectively, are apparently found.

© 2005 Elsevier Ltd. All rights reserved.

---

## 1. Introduction

Direct noise computation (DNC) consists of calculating the sound field directly by solving the unsteady compressible flow equations [1]. It is intended to allow investigations of noise generation mechanisms by providing both flow and sound fields. This motivation is strong for flows such as subsonic jets where noise sources are still not clearly identified. For performing DNC, direct numerical simulation (DNS), which involves the full resolution of the Navier–Stokes equations, can be used [2] but its applications are limited to low Reynolds number flows displaying a small range of turbulent scales. Such a restriction does not exist with large eddy simulation (LES) which can theoretically deal with flows at any Reynolds number by calculating only

the scales larger than the grid size. For this reason, LES appears to be an appropriate tool to investigate realistic turbulent flows. It has been tested over the last few years to study the noise radiated by supersonic [3] and subsonic [4–8] round jets. The latter simulations demonstrated the feasibility of DNC for subsonic jets using LES, but moderate Reynolds numbers were often involved. For example, the first jet simulated by the authors [4] was for a Mach number of  $M = u_j/c_a = 0.9$  and for a Reynolds number of  $Re_D = u_j D/v = 6.4 \times 10^4$  ( $u_j$  is the jet nozzle exit,  $c_a$  the ambient sound speed,  $D$  the jet diameter, and  $v$  the molecular viscosity). To discuss the full physics of jet noise, dealing with higher Reynolds numbers now appears necessary.

With this aim in view, the LES of a high Reynolds number, subsonic circular jet, developing in an air at standard conditions, is carried out. The jet is isothermal with a jet centerline temperature  $T_j = T_a$  ( $T_a$  is the ambient temperature). The Mach number is  $M = 0.9$  and the Reynolds number is  $Re_D = 4 \times 10^5$ . Two simulations are

<sup>\*</sup> Corresponding author. Tel.: +33 4 72 18 60 18; fax: +33 4 72 18 9143.

E-mail address: christophe.bogey@ec-lyon.fr (C. Bogey).

carried out using grids of different size, one extending far away downstream and one including a part of the acoustic field. They are performed with a high accuracy using a Navier–Stokes solver (ALESIA [4,9]) developed for DNC using non-reflecting boundary conditions [10] and updated with new low-dispersive and low-dissipative numerical schemes [11]. The first motivation is to show that the flow development is not dependent on the location of the grid boundaries. The second is to obtain by LES flow and sound field properties in agreement with those typically found for jets with similar high Reynolds numbers. This would indicate that the effective Reynolds number of the simulated jet is preserved by the numerical resolution, i.e. that it corresponds to the Reynolds number  $Re_D$  defined by the flow initial conditions, which is one key point in the development of reliable LES for realistic flows.

In the present work involving a high Reynolds number jet, the simulations are based on the LES approach consisting of taking into account the effects of the turbulent-energy dissipating scales, not resolved by the grid, through a filtering applied explicitly to the flow variables instead of an eddy-viscosity model as usually. This approach is recent but successful applications to isotropic turbulence and channels flows have now been presented [12–14]. Its original feature is to use selective/compact filtering, designed to eliminate short waves such as the grid-to-grid oscillations without affecting the large resolved scales unlike an eddy viscosity. Thanks to this selectivity, the LES results are expected to be independent of the filtering. To assess this original LES approach, the jet features obtained from the present simulations are systematically compared to corresponding measurements. The sound field properties are especially investigated since typical properties are observed experimentally for high Reynolds number jets, with for instance broadband sound spectra [15] in the sideline direction. The final purpose of this work is to provide a numerical database for further investigations dealing with the influence of different simulation parameters on the radiated noise [16,17] or with noise generation mechanisms [18].

The present paper is organized as follows. The governing equations and the numerical procedure are presented in Section 2. The simulation parameters, and snapshots of vorticity and pressure are shown in Section 3 where the independence of the results from the filtering procedure is also studied. The flow field and the sound field provided directly by LES are then investigated in Sections 4 and 5, respectively. The flow fields obtained on the two grids are compared to each other, while all flow and acoustic results are examined with respect to measurements in the literature. Concluding remarks are then given in Section 6. Finally, a selective filter implemented in the present simulations is provided in Appendix A.

## 2. Governing equations and numerical procedure

### 2.1. Governing equations

For LES of compressible flows, the basic governing equations are the filtered Navier–Stokes equations, which can be written as [19]:

$$\begin{aligned} \frac{\partial \bar{\rho}}{\partial t} + \frac{\partial}{\partial x_j} (\bar{\rho} \bar{u}_j) &= 0 \\ \frac{\partial}{\partial t} (\bar{\rho} \bar{u}_i) + \frac{\partial}{\partial x_j} (\bar{\rho} \tilde{u}_i \tilde{u}_j + \bar{p} \delta_{ij} - \tilde{\tau}_{ij} - \mathcal{T}_{ij}) &= 0 \\ \frac{\partial}{\partial t} (\bar{\rho} \tilde{e}) + \frac{\partial}{\partial x_j} ((\bar{\rho} \tilde{e} + \bar{p}) \tilde{u}_j - \tilde{\tau}_{ij} \tilde{u}_i + \tilde{q}_j + \mathcal{Q}_j) - \tilde{u}_i \frac{\partial \mathcal{T}_{ij}}{\partial x_j} &= 0 \end{aligned}$$

where the flow variables  $\rho$ ,  $u_i$  and  $p$  are the density, velocity and pressure. The overbar denotes a filter operation, which commutes with the partial derivatives. The tilde indicates that the quantity is based on filtered variables, e.g. for the velocity  $\tilde{u}_i = \bar{\rho} \bar{u}_i / \bar{\rho}$  (Favre filter operator), and for the total energy  $\bar{\rho} \tilde{e} = \bar{p} / (\gamma - 1) + \bar{\rho} \tilde{u}_k \tilde{u}_k / 2$  where  $\gamma$  is the specific heat ratio.

The resolved viscous stress tensor  $\tilde{\tau}_{ij}$  is defined by  $\tilde{\tau}_{ij} = 2\mu(\tilde{S}_{ij} - \tilde{S}_{kk}\delta_{ij}/3)$  where  $\tilde{S}_{ij} = (\partial \tilde{u}_i / \partial x_j + \partial \tilde{u}_j / \partial x_i)/2$  and  $\mu$  is the molecular dynamic viscosity. The heat flux is given by  $\tilde{q}_j = -\lambda \partial \tilde{T} / \partial x_j$  where the temperature  $\tilde{T}$  is deduced from the filtered density and pressure using the state equation  $\bar{p} = \bar{\rho} r \tilde{T}$ , and  $\lambda = \mu c_p / \sigma$  is the thermal conductivity ( $\sigma$  is the Prandtl number, and  $c_p$  is the specific heat at constant pressure). The filtering of the Navier–Stokes equations makes different terms appear [19]. These terms are referred to as subgrid terms since they cannot be directly calculated from the resolved variables. Among them, the two following ones are usually kept: the subgrid turbulent stress tensor  $\mathcal{T}_{ij} = \bar{\rho} \tilde{u}_i \tilde{u}_j - \bar{\rho} \bar{u}_i \bar{u}_j$  and the pressure–velocity subgrid term  $\mathcal{Q}_j = -(\bar{p} \tilde{u}_j - \bar{\rho} \bar{u}_j) / (\gamma - 1)$ .

The modelling of the subgrid stress tensor has been debated for a long time, see discussions in recent reviews [20–23]. Since the energy-dissipating scales are not resolved, it is generally agreed that the addition of an artificial damping is required. This is classically done through subgrid models based on an eddy-viscosity hypothesis and designed from physical considerations to express the  $\mathcal{T}_{ij}$ , such as for the famous Smagorinsky model [24]. However, since the eddy viscosity has the same functional form as the molecular viscosity, it is difficult to define the effective Reynolds number of the simulated flows [17,25]. An alternative to the eddy viscosity is to damp the turbulent energy using numerical dissipation. This is the case in the MILES approach [26] where the dissipation is provided implicitly by the numerical scheme. Successful applications of this approach have been shown [27] but the question about the damping effects on the resolved scales remains as

long as dissipative numerical methods such as shock-capturing schemes [28] are used.

In the present LES, a numerical approach different from MILES is followed. The Navier–Stokes equations are solved using low-dissipative schemes while a selective filtering is applied explicitly to the density, the momentum  $\rho u_i$  and the pressure, to remove the high wave numbers close to the grid cut-off wave number. The two subgrid terms are taken to be  $\mathcal{T}_{ij} = 0$  and  $\mathcal{Z}_j = 0$ . The selective filtering is optimized to eliminate grid-to-grid oscillations without affecting significantly the scales discretized by more than four grid points. It is thus useful to distinguish two cut-off wave numbers in the present LES: the grid cut-off wave number for two points per wavelength,  $k_c^g = \pi/\Delta x$  ( $\Delta x$  is the grid size), and the filtering cut-off wave number  $k_c^f = \pi/(2\Delta x)$ . The resolved, the filtered and the subgrid scales can then be defined as in Fig. 1. The resolved scales here do not denote all the scales discretized by the grid as usual, but those calculated accurately by the numerical algorithm and not appreciably affected by any artificial dissipation. To demonstrate the efficiency of the LES approach based on explicit filtering, simulations of well-documented configurations such as isotropic turbulence and channel flows [12,13] have been carried out. The present work is an extension of these works for a flow at a high Reynolds number. Theoretical developments have also been proposed to bring support to this approach [14]. Finally note that there is no opportunity for backscatter, the transfer of energy from the unresolved to the resolved scales, using this method. This can be considered of little importance for free shear flows such as the jet presently simulated, but this issue will need further investigations for bounded shear flows.

## 2.2. Numerical methods

The discretization of the flow equations is performed with a 13-point stencil finite-difference scheme for the

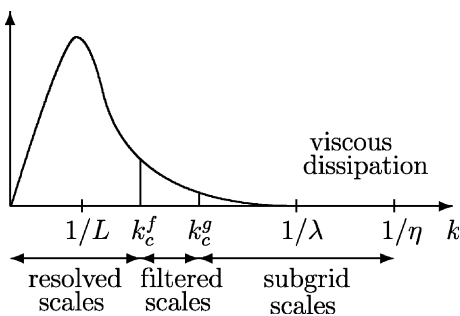


Fig. 1. Schematic representation of the spectrum of turbulent kinetic energy  $E(k)$  with the wave numbers associated to the integral, Taylor and Kolmogorov scales,  $L$ ,  $\lambda$  and  $\eta$ , and with the filtering and grid cut-off wave numbers,  $k_c^f$  and  $k_c^g$ . The resolved and the filtered scales are the scales supported by the grid.

spatial derivation and with a six-stage low-storage Runge–Kutta algorithm for the time integration. Both schemes [11] have been developed to display optimized properties in the Fourier space so that fluctuations discretized by more than four points per wavelength are neither distorted nor dissipated.

Selective filterings designed to eliminate grid-to-grid oscillations without affecting the resolved scales are used to ensure numerical stability and to take into account the subgrid dissipation as discussed in the previous section. They are applied explicitly to the density, momentum and pressure every two iterations, sequentially in the  $x$ ,  $y$  and  $z$  Cartesian directions and in the diagonals of the  $xy$ ,  $xz$  and  $yz$  sections. In the Cartesian directions, the filtering is performed using a 13-point stencil filter [11] optimized up to four points per wavelength. For instance, the filtering in the  $x$ -direction writes

$$U_{i,j,k}^f = U_{i,j,k} - \sigma_d \sum_{l=-6}^6 d_l U_{i+l,j,k}$$

where  $U = \{\rho, \rho u, \rho v, \rho w, p\}$ ,  $U^f$  is the filtered variable,  $d_l$  are the filter coefficients and  $\sigma_d = 2/3$ , arbitrarily. In the diagonals, the filtering is carried out using the filter described in Appendix A. Thus in the  $xy$ -direction

$$U_{i,j,k}^f = U_{i,j,k} - \sigma_d \sum_{l=-10}^{10} d_l^d U_{i+l,j+l,k}$$

with the coefficients  $d_l^d$  provided in Appendix A and  $\sigma_d = 2/3$  as previously. Note that this diagonal filtering is not applied near the boundaries. It is moreover not strictly necessary for stability and it is not used in the latest LES performed in our group. The value of  $\sigma_d$  and the frequency of filtering are arbitrary but they are expected to have a negligible influence on the flow results thanks to the selectivity of the filters. This important point is addressed in Section 3.4.

The implementation of the spatial schemes was discussed in a previous paper [11]. The high accuracy of the schemes was shown to be preserved for the stretching rate of 2% applied to the mesh spacing in the present LES in order to use different discretizations inside and outside the jet flow. Their connection with the boundary conditions was also described. It consists of decreasing progressively the size of the scheme stencil from the interior to the boundary points where standard fourth-order non-centered schemes are used.

## 3. Simulation parameters and results

### 3.1. Jet inflow

A circular isothermal jet developing in an air at standard sea level temperature and pressure is investigated. The jet Mach number is  $M = u_j/c_a = 0.9$ , which is of

interest for aeronautic applications, and is also appropriate to keep the computation at an affordable cost. It corresponds also to a value found in a large number of experimental studies of the literature, providing both aerodynamic [29–32] and acoustic [15,33,34] results. The jet Reynolds number is  $Re_D = 4 \times 10^5$  which is quite high with respect to the range of Reynolds numbers usually considered in LES ( $10^3 \leq Re_D \leq 10^5$ ).

For high Reynolds numbers  $Re_D \geq 10^5$ , the jet exit boundary layers are very thin [35] with a momentum thickness of the order of  $10^{-3}D$ , and the number of points necessary for its discretization would be exorbitant. Therefore in the present simulation, the jet inflow conditions have been modeled by imposing mean flow profiles while using a random excitation to seed the turbulence. The inflow mean longitudinal velocity  $u_0(r)$  is given by the following hyperbolic-tangent profile

$$\frac{u_0(r)}{u_j} = \frac{1}{2} + \frac{1}{2} \tanh\left(\frac{r_0 - r}{2\delta_\theta}\right)$$

where  $u_j$  is the inflow centerline velocity,  $\delta_\theta$  the initial momentum thickness of the annular shear layer, and  $r_0$  the jet radius. Pressure is taken as the ambient pressure, radial and azimuthal velocities are set to zero. The inflow mean density profile is given by the Crocco–Busemann relation

$$\frac{\rho_0(r)}{\rho_j} = \left(1 + \frac{\gamma - 1}{2} M^2 \frac{u_0(r)}{u_j} \left(1 - \frac{u_0(r)}{u_j}\right)\right)^{-1}$$

for an isothermal jet. The profiles of the inflow longitudinal velocity and density thus obtained are represented in Fig. 2. The ratio between the jet radius and the shear-layer momentum thickness  $r_0/\delta_\theta$  is directly connected to the number of grid points in the jet diameter, and is therefore clearly limited in three-dimensional simulations. The present ratio is chosen as  $r_0/\delta_\theta = 20$ , which is large enough to allow the development of turbulent structures in the shear zone.

To start the turbulent flow development, the jet is forced by adding random velocity fluctuations to the

mean profile, in the shear zone for  $x \simeq r_0$ . The forcing procedure applied is this described for an early jet simulation [4]. Two parameters are however modified with respect to this simulation: the first 16 azimuthal modes are involved in the forcing, and the amplitude coefficient is  $\alpha = 0.007$ . This excitation introduces solenoidal velocity fluctuations with a low magnitude so that it does not generate significant spurious sound waves. These fluctuations are also poorly correlated azimuthally as shown in Fig. 3.

### 3.2. Numerical specifications

The Cartesian grids used for the two simulations, referred to as LESaero and LESac in what follows, are represented in Fig. 4, and contain, respectively, 16.6 and 12.5 million points. For the two grids, the discretizations in the  $y$  and  $z$  directions are the same and are symmetrical about the jet axis. The grids of LESaero and LESac are identical in the inner zone defined by  $0 \leq x \leq 25r_0$  and  $-10r_0 \leq y, z \leq 10r_0$ . The transverse mesh spacing is uniform for  $y, z \leq 2r_0$  with  $\Delta y_0 = \Delta z_0 = r_0/15$ , and then increases at a rate of 2% to reach  $y, z = 13r_0$  in LESaero and  $y, z = 16r_0$  in LESac. The axial mesh spacing is constant with  $\Delta x = 2\Delta y_0$  for  $0 \leq x \leq 25r_0$  and then increases progressively at a rate of 0.4% in LESaero. The flow field is thus calculated up to  $x = 60r_0$  in LESaero but only up to  $x = 25r_0$  in LESac. The near acoustic field is only investigated in LESac. In this case, the transverse mesh spacing reaches a maximum value of  $\Delta y = 0.4r_0$  well outside the jet, which corresponds to a cut-off Strouhal number of about 2 for the sound field. With this cut-off Strouhal number, the loss in total dB is expected to be less than 0.5 dB at every radiation angle, as suggested by experimental sound spectra [36].

Parameters of the two simulations such as the time periods used for computing flow and sound quantities are presented in Table 1. The time step is  $\Delta t = 0.85\Delta y_0/c_a$  for the two simulations. The computation time and consequently the different sampling times are

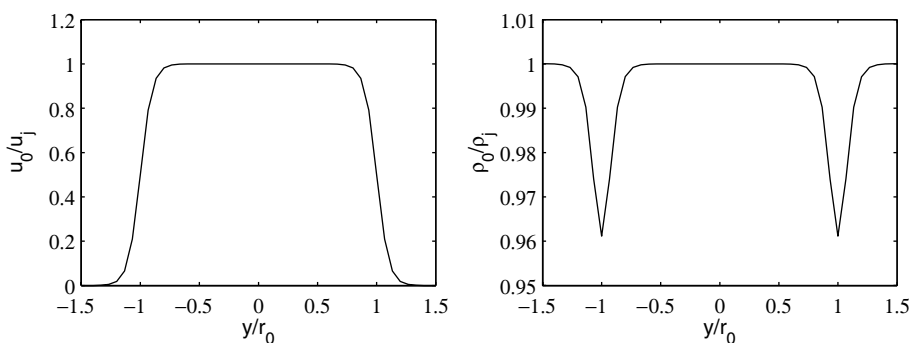


Fig. 2. Transverse profiles of the inflow mean velocity and density,  $u_0/u_j$  and  $\rho_0/\rho_j$ , at  $x = 0$  and  $z = 0$ .

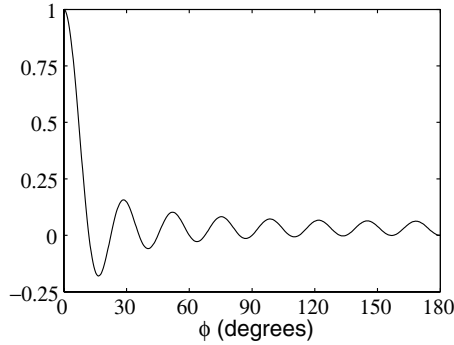


Fig. 3. Azimuthal cross-correlation of the forcing velocity disturbances.

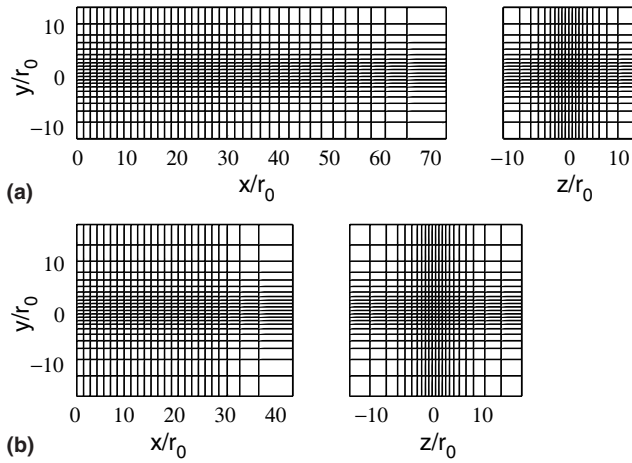


Fig. 4. Visualization of the  $x-y$  and  $y-z$  sections of the grids for: (a) LESaero and (b) LESac. Only every 10th line is shown.

long enough to achieve statistical convergence. To illustrate this, the sound field in LESac is for example studied during a period  $T_{\text{ac}}$  which can be associated with a minimum Strouhal number of  $D/(T_{\text{ac}} u_j) \simeq 1.2 \times 10^{-3}$ .

Table 1  
Grid and time parameters of the simulations LESaero and LESac

	LESaero	LESac
$n_x \times n_y \times n_z$	$395 \times 205^2$	$255 \times 221^2$
Sim. time $T$	$7 \times 10^4 \Delta t$	$4 \times 10^4 \Delta t$
$T$	$3970 r_0 / c_0$	$2270 r_0 / c_0$
$D/(Tu) \sim St$	$5.6 \times 10^{-4}$	$9.9 \times 10^{-4}$
Flow for	$x \leq 60r_0$	$x \leq 25r_0$
Mean flow s.t.	$6.2 \times 10^4 \Delta t$	$3.6 \times 10^4 \Delta t$
Turb. int. s.t.	$4 \times 10^4 \Delta t$	$2.5 \times 10^4 \Delta t$
$u'$ -spectra s.t.	$6 \times 10^4 \Delta t$	$3.5 \times 10^4 \Delta t$
Sound for	—	$x \leq 30r_0$
s.t.	—	$3.3 \times 10^4 \Delta t$
CPU time (h)	200	90

sim. is used for simulation, s.t. for sampling time, turb. int. for turbulence intensities,  $u'$  is the fluctuating axial velocity. The CPU time is for a Nec SX5.

### 3.3. Boundary conditions

To minimize the amplitude of the acoustic waves reflected at the limits of the computational domain, non-reflective boundary conditions are used. The radiation and the outflow boundary conditions based on a formulation of sound waves in the acoustic far-field [10] are implemented in three rows of points, as shown in Fig. 5. A sponge zone combining grid stretching and Laplacian filtering [10] is added in the downstream region to dissipate flow fluctuations before they reach the boundary.

Moreover, since the radiation and the outflow boundary conditions rely on equations written for the fluctuating quantities alone, the mean quantities might drift. Small adjustment terms have therefore been added to impose their values at the boundaries. Practically, they are integrated at every iteration, explicitly, in the following way

$$U^r = (1 - \sigma_r)U + \sigma_r U_{\text{ref}}$$

with  $U = \{\rho, u, v, w, p\}$ ,  $U_{\text{ref}} = U_{\text{inflow}} = \{\rho_0, u_0, v_0, w_0, p_0\}$  and  $\sigma_r = 5 \times 10^{-2}$  at the jet inflow,  $U = \{\rho, p\}$ ,  $U_{\text{ref}} = \{\rho_a, p_a\}$  and  $\sigma_r = 5 \times 10^{-3}$  outside the flow,  $U^r$  representing the modified variables. In this way, all the mean variables at the jet inflow are set to the initial flow values, denoted by the subscript 0. Outside the flow, only the mean density and pressure are imposed. They are set to the ambient density and pressure denoted by the subscript a. Furthermore the factor  $\sigma_r$  is small to avoid sound reflections. Finally note that this method is very similar to the methods proposed by Rudy and Strikwerda [37] and by Poinsot and Lele [38] to specify the steady-state solution at non-reflecting boundaries in compressible simulations.

### 3.4. Instantaneous vorticity and pressure

Fig. 6 displays instantaneous snapshots of LES quantities provided by the two simulations. For LESaero, the axial section of the vorticity norm  $|\omega|$  is shown in Fig. 6(a). For LESac, axial and transverse sections are shown in Fig. 6(b), with the vorticity  $|\omega|$  in the turbulent flow region and the fluctuating pressure  $p'$  outside.

The vorticity fields show a large range of vortical scales, with the presence of a fine turbulence as expected for a high Reynolds number. The axial sections illustrate the flow development from shear layers to a turbulent jet, with a jet spreading which is especially visible far downstream for the LESaero simulation in Fig. 6(a). The shear layers appear to interact in the vicinity of  $x = 10r_0$ . The length of the potential core is therefore about  $10r_0$ , which is comparable to the values measured on corresponding jets [29].

The snapshots of the pressure field in Fig. 6(b) demonstrate that the noise generated by the jet is well taken

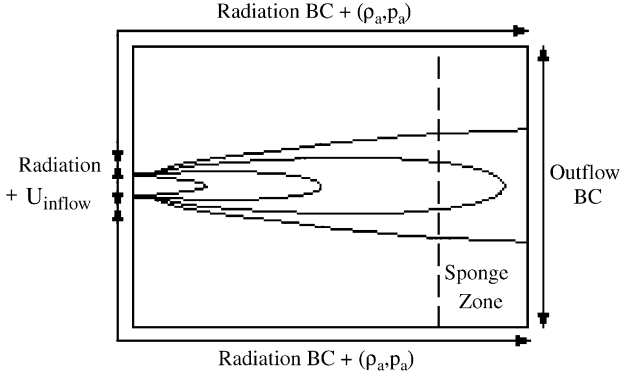
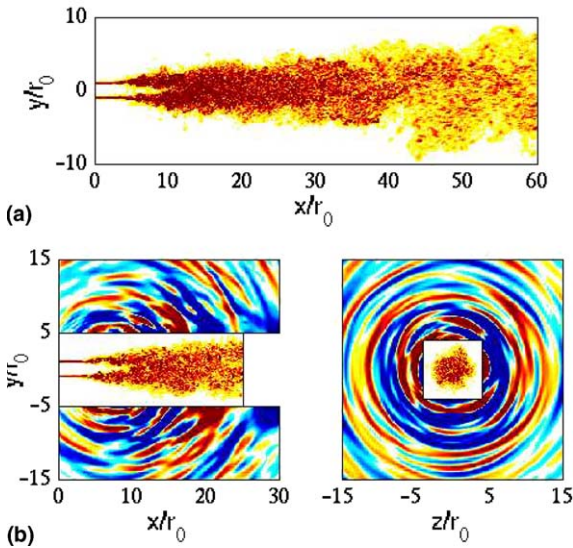


Fig. 5. Sketch of the boundary conditions.

Fig. 6. (a) LESaero: snapshot of the vorticity  $|\omega|$ . The color scale is from 0 to  $4 \times 10^4 \text{ s}^{-1}$ . (b) LESac: snapshots of the vorticity  $|\omega|$  in the flow and of the fluctuating pressure  $p'$  outside. Left: in the  $x-y$  plane at  $z = 0$ . Right: in the  $y-z$  plane at  $x = 11r_0$ . The grey scales are from 0 to  $8 \times 10^4 \text{ s}^{-1}$  for the vorticity and from -70 to 70 Pa for the pressure.

into account by the simulation. It is properly propagated outside of the flow, and is contaminated neither by the inflow forcing, nor by possible reflections at the boundaries. The axial section shows sound waves originating from a region located in the vicinity of the end of the potential core, in agreement with experimental observations [36]. The acoustic radiation is also more pronounced in the downstream direction, as expected. The transverse section shows the structure of the sound waves. Partially circular waves are found in the considered section at  $x = 11r_0$ .

### 3.5. Independence from the filtering

The use of an artificial dissipation in LES is aimed at dissipating energy which is transferred, following the

turbulent cascade process, from the large to the small scales, and therefore might accumulate at the high wave numbers, corresponding typically to the grid-to-grid oscillations, and lead to the divergence of the simulation. An important issue is to apply damping procedures which do not dissipate the turbulence too much or, in other words, to minimize their effects on the large scales. To closely control the amount of dissipation, regularization procedures [39] have then been proposed where the parameters of the dissipation are adjusted from the turbulence just enough to avoid growth of energy at high wave numbers. Such procedures are similar to the dynamic procedures developed for the eddy-viscosity model and might be computationally expensive. Several parameters are also to be fixed when compact/selective filtering is used as artificial dissipation. The filtering can indeed be applied every  $M$  iterations or  $m$  times per iteration, with a coefficient  $\sigma_d$  between 0 and 1. These parameters  $M$ ,  $m$  and  $\sigma_d$  are likely to be determined by regularization, but practically they are arbitrarily chosen to ensure numerical stability, which raises questions about the dependence of the results on the filtering procedure.

The sensitivity of LES results to the filtering should however depend on the filter properties. Visbal and Rizetta [12] have for instance shown that low-order filters provide excessive dissipation for decaying isotropic turbulence and that at least sixth-order is required to obtain correct results. Another example of the effects of filtering in LES is given by Uzun et al. [7] who reported that the features of a circular jet can vary according to the filters used. In the present simulations, the filters are sufficiently selective that one can expect the filtering to exert no significant influence on the resolved scales discretized by more than four grid points. Energy is only diffused when it is transferred from the resolved to the filtered scales, represented in Fig. 1. The resolved scales are the major energy-containing scales and determine the amount of energy to be dissipated. The dissipation rate, and consequently the LES results, should therefore be independent of the filtering procedure.

To show the negligible influence of the filtering on the LES fields, we can change the filtering coefficient or its application frequency, obtaining similar results. Here a simulation characterized by the parameters of the LESac simulation but where the filtering is applied every three iterations instead of every two iterations is performed. This simulation, referred to as LESac2, provides jet flow and sound fields with properties very similar to those from LESac. For instance, an excellent agreement is observed for the mean flow development, the turbulence intensities, the velocity spectra and length scales, and for the sound levels and spectra. Illustrations are presented in Fig. 7(a) and (b) displaying centerline profiles of the rms axial-velocity fluctuations and sideline acoustic levels from LESac and LESac2. These

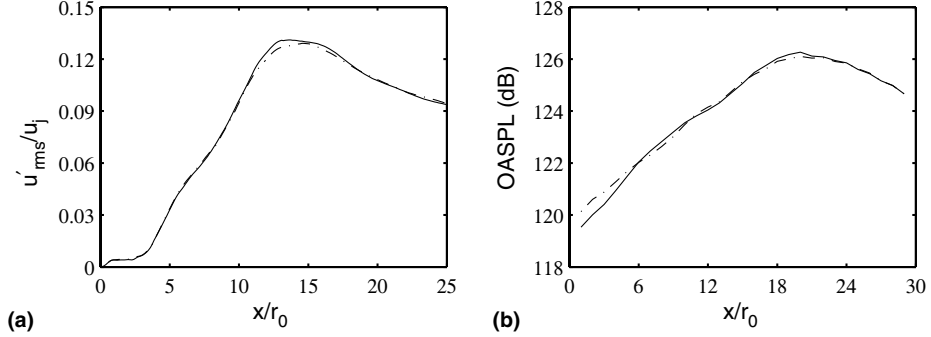


Fig. 7. (a) Centerline profiles of the rms-value of the fluctuating axial velocity, and (b) overall sound pressure levels for  $r = 15r_0$ , obtained from: (—) LESac, (---) LESac2.

results from simulations where the filtering is applied quite differently support that the turbulence does not depend much on the filter application parameters, and that regularization procedures may appear unnecessary when the filters are selective enough.

#### 4. Flow field

In this section, the flow fields computed by the LESaero and LESac simulations are investigated. Comparisons between the two, and with experimental data, are made.

##### 4.1. Mean flow

Streamlines originating from the mesh boundaries are presented in Fig. 8(a) for LESaero and in Fig. 8(b) for LESac. They illustrate the entrainment of the surrounding fluid in the jet, and demonstrate that the boundary

conditions are appropriate for the incoming of fluid into the computational domain in both simulations. The streamlines are fairly parallel to the jet near the inflow, but more perpendicular to the flow direction as the axial distance increases and as the jet becomes turbulent. This is in good agreement with experimental observations [40].

To study the mean flow more quantitatively, the axial profiles of the centerline velocity  $u_c$  and of the jet half-width  $\delta_{0.5}$  are represented in Fig. 9(a) and (b). The profiles obtained from LESaero and from LESac are fairly superposed, which demonstrates that the mean flows computed using computational domains of different sizes are very close, and do not appreciably depend on the location of the mesh boundaries. As expected according to the vorticity snapshots, the velocity decay starts at the end of the potential core for about  $x \simeq 10r_0$  in Fig. 9(a). The decay is successfully compared with the one measured by Lau et al. [29] for a high- $Re_D$  jet at Mach 0.9. A small deceleration of the centerline velocity is also detected for about  $x = 5r_0$ . It is interesting to notice that this behaviour within the potential core has been observed experimentally [41]. Moreover, the evolution of the jet half-width in Fig. 9(b) shows that the jet spreads slowly before the end of the potential core, but quite rapidly and apparently linearly after. There is also a fair agreement with measurements provided by Zaman [42] for a  $M = 0.5$  jet in the region just after the end of the potential core. Note that all measurements are shifted in the downstream direction for the comparisons, to deal with their different core lengths which can vary according to their respective nozzle exit conditions.

In the jet literature, the mean flow is usually investigated far downstream from the nozzle, for  $x > 60r_0$  at least [43], where the self-similarity of the mean profiles is observed. In this zone, the velocity decay and the jet spreading are characterized by two parameters: the decay constant  $B$  and the spreading rate  $A$ , such as  $u_o/u_j = B \times (2r_0/(x - x_0))$  and  $\delta_{0.5} = A \times (x - x_0)$ . In the present study, since the self-similarity may not be reached owing to the limited size of the computational

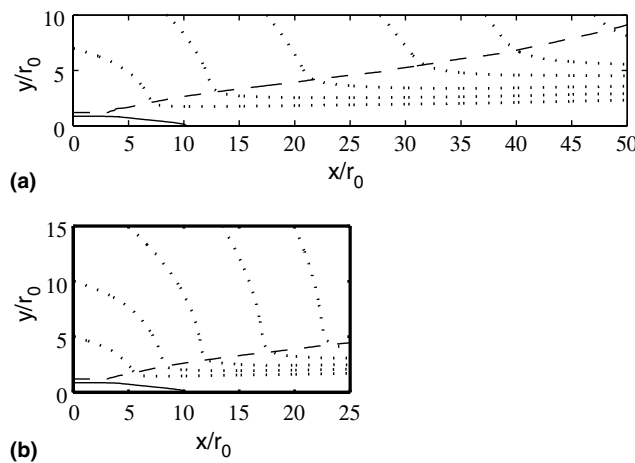


Fig. 8. Visualization of the mean velocity fields in the  $x$ - $y$  plane at  $z = 0$  for: (a) LESaero, (b) LESac. (—) contour associated with the mean axial velocity  $0.95u_j$ , (---) contour associated with  $0.03u_c$  ( $u_c$  is the mean centerline velocity), (···) mean streamlines.

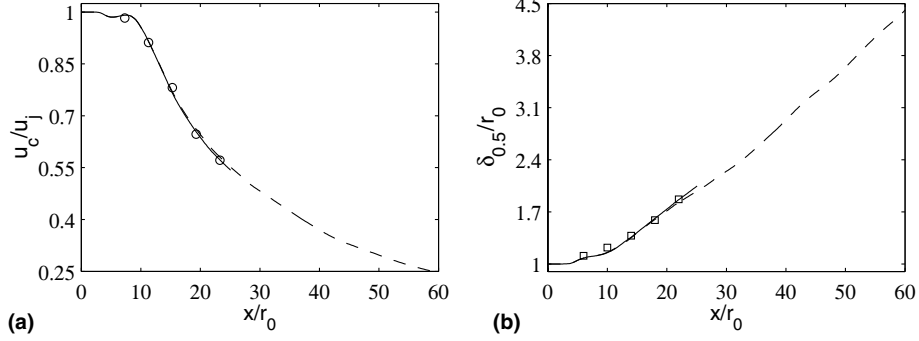


Fig. 9. Axial profiles, (a), of the mean centerline velocity  $u_c/u_j$  and (b), of the jet half-width  $\delta_{0.5}/r_0$  for: (—) LESAero and (—) LESac. Measurements: (○) Lau et al. [29] ( $M = 0.9$ ,  $Re_D = 10^6$ ), (□) Zaman [42] ( $M = 0.5$ ,  $Re_D = 3 \times 10^5$ ), shifted respectively by  $-4.7r_0$  and  $2r_0$  in the axial direction to match the different core lengths.

domain, the local decay constant  $B = (1/2)[d(u_j/u_c)/d(x/r_0)]^{-1}$  and the local spreading rate  $A = d\delta_{0.5}/dx$  are calculated and they are given in Fig. 10(a) and (b) for  $20r_0 \leq x \leq 60r_0$ . The variations of  $B$  and  $A$  with the axial distance indicate clearly that the self-preserving jet zone is not reached and would require a mesh extending further downstream. However, it appears also that  $B$  and  $A$  may tend to values of about 6 and 0.09, respectively, as  $x$  increases. These asymptotic values are in accordance with the values of  $B$  and  $A$  measured in the jet self-similarity region [44,45]. This agreement with the self-similarity constants near the end of the computational domain led us to plot the mean velocity profile for  $x = 50r_0$  in Fig. 11. It compares well with that measured in experiments far downstream from the nozzle. The mean flow obtained by LES is therefore in agreement with experimental data both for the transitional region after the end of the potential core and for the self-similarity region likely to be found further downstream.

#### 4.2. Turbulence intensities

The centerline profile and the radial profile for  $x = 20r_0$  of the turbulent axial velocity  $\langle u'u' \rangle^{1/2}/u_j$ ,

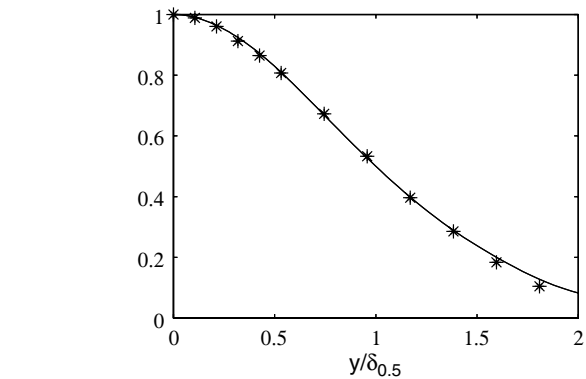


Fig. 11. Radial profiles of the mean axial velocity  $\langle u \rangle/u_c$ : (—) obtained from LESAero at  $x = 50r_0$ , (\*) measurements of Panchapakesan and Lumley [44] ( $M = 0.08$ ,  $Re_D = 1.1 \times 10^4$ ) in the jet self-similarity region.

where the prime denotes the fluctuating quantity and  $\langle \cdot \rangle$  the time average, are plotted in Fig. 12(a) and (b), for LESAero and LESac. Results provided by the two simulations are in good accordance, and this is especially striking for the radial profiles in Fig. 12(b) which are very close. As for the mean flow, the location of the boundaries does not significantly affect the development

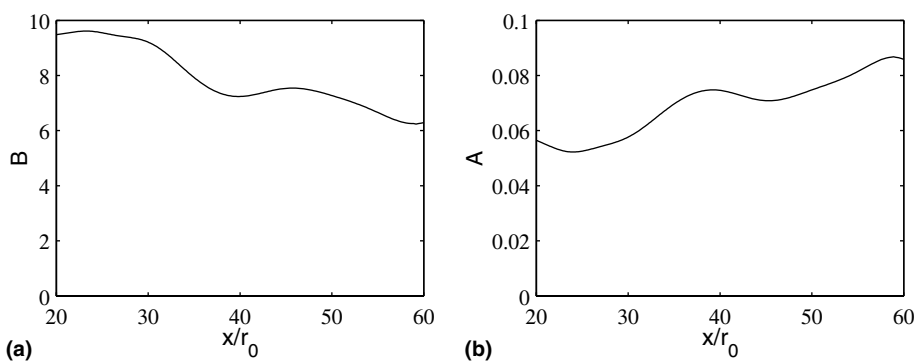


Fig. 10. Axial profiles from LESAero, (a), of the local centerline velocity decay constant  $B = (1/2)[d(u_j/u_c)/d(x/r_0)]^{-1}$  and (b), of the local spreading rate  $A = d\delta_{0.5}/dx$ .

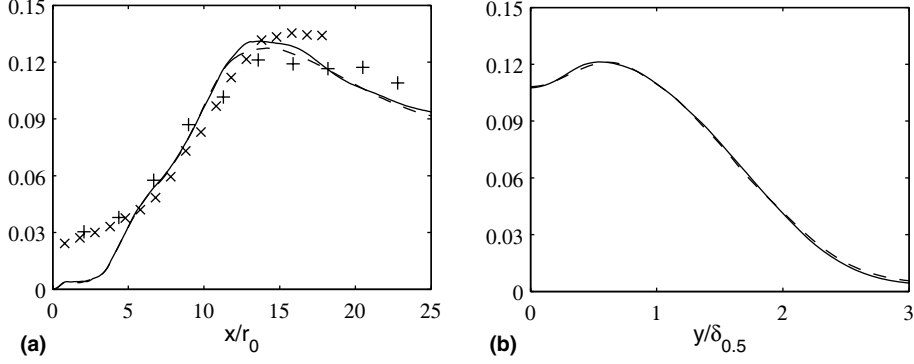


Fig. 12. (a) Centerline profile and (b) radial profile for  $x = 20r_0$  of the turbulent axial velocity  $\langle u'u' \rangle^{1/2}/u_j$  for: (—) LESaero, (—) LESac. Measurements: (x) Jordan et al. [31] ( $M = 0.9$ ,  $Re_D = 10^6$ ), (+) Arakeri et al. [32] ( $M = 0.9$ ,  $Re_D = 5 \times 10^5$ ), shifted respectively by  $-4.2r_0$  and  $-7.1r_0$  in the axial direction to match the different core lengths.

of the turbulence in the jet. The axial profile in Fig. 12(a) reaches a peak for about  $x = 14r_0$ , slightly after the end of the potential core, in the transitional region where the turbulent shear layers merge. The increase and the peak value are compared successfully to recent particle image velocimetry (PIV) measurements on Mach number  $M = 0.9$ , similar Reynolds number jets. These comparisons support that the jet transition is well described by the simulation. This is of importance for the direct noise computation, since the end of the potential core is known to be a region of significant noise generation [4].

For the study of the zone downstream from the core, the turbulence intensities are investigated. They are given by the ratios between the fluctuating velocities and the local centerline mean velocity. In a high Reynolds number jet, experiments [43] have shown that they become self-similar only around 100 radii downstream from the nozzle, where for example  $\langle u'u' \rangle^{1/2}/u_c \simeq 0.25$  on the jet axis [44,45]. In the present simulation, the self-similarity plateau may therefore not be reached, which is supported by the centerline profile of  $\langle u'u' \rangle^{1/2}/u_c$  presented in Fig. 13(a). This quantity increases regularly in the same way as in the experiment of Arakeri

et al. [32], and tends to a value in agreement with the measured self-similar value of 0.25. The radial profiles of the turbulence intensities for  $x = 50r_0$  are then represented in Fig. 14. They agree fairly well with experimental profiles measured in the self-preserving region.

#### 4.3. Integral length scales

The integral length scales on the jet axis are now investigated. For this, the correlation function of the axial fluctuating velocity  $R_{11}^{(1)}(r)$  is calculated for points located at  $(x, y = z = 0)$  by

$$R_{11}^{(1)}(r) = \frac{\langle u'(x + r/2)u'(x - r/2) \rangle}{\langle u'^2(x + r/2) \rangle^{1/2} \langle u'^2(x - r/2) \rangle^{1/2}}$$

and the longitudinal length scale is given by  $L_{11}^{(1)} = \int_0^\infty R_{11}^{(1)}(r)dr$ .

The centerline length scales obtained for the present simulated jet are presented in Fig. 15 in the turbulent region after the potential core, for  $10r_0 \leq x \leq 60r_0$ . First, there is no significant difference between the length scales provided by the simulations LESaero and LESac. Second, and this is an important key point, the length scales increase apparently linearly as observed experimentally, with a good agreement with the law measured by Wygnanski and Fiedler [43]. This validates the two-point correlations of the velocity field computed by LES, and demonstrates that the jet spreading occurs with a relevant increase of the size of the turbulent scales. Note that slight differences are noticed with respect to the linear increase of the length scales. They might be generated by small oscillations shown by the spatial correlation functions for large separation distances due to convergence issues.

#### 4.4. Velocity spectra

The one-dimensional spectra of the  $u'$ -velocity  $E_u^{(1)}(k_1)$  are presented in Fig. 16 for  $x = 20r_0$  and

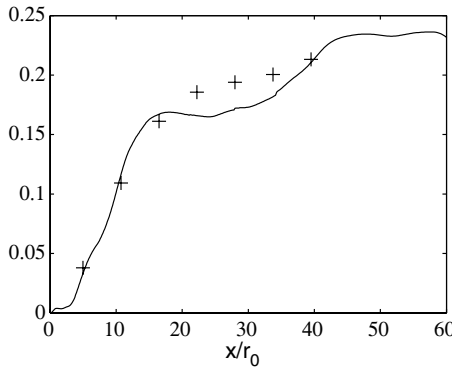


Fig. 13. Centerline profiles of the turbulence intensity  $\langle u'u' \rangle^{1/2}/u_c$ : (—) from LESaero, (+) measurements of Arakeri et al. [32] ( $M = 0.9$ ,  $Re_D = 5 \times 10^5$ ) shifted by  $-7.1r_0$  in the axial direction as in Fig. 12.

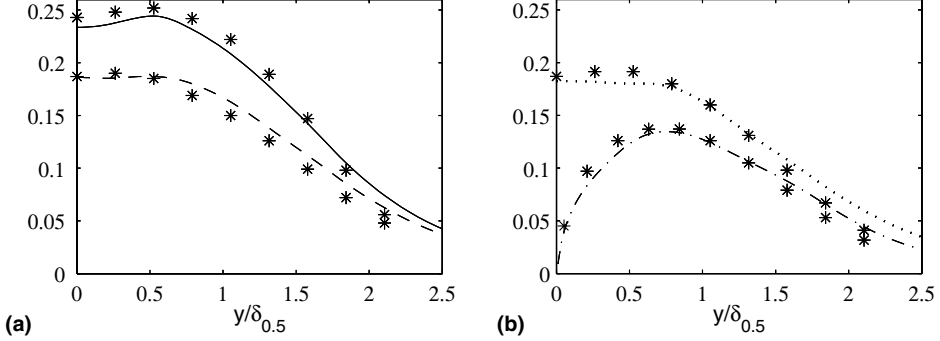


Fig. 14. Radial profiles for  $x = 50r_0$  of the turbulence intensities for LESaero: (—)  $\langle u' u' \rangle^{1/2} / u_c$  (---)  $\langle v' v' \rangle^{1/2} / u_c$ , (···)  $\langle w' w' \rangle^{1/2} / u_c$  and (- - -)  $\langle u' v' \rangle^{1/2} / u_c$ . (\*) measurements of Panchapakesan and Lumley [44] ( $M = 0.08$ ,  $Re_D = 1.1 \times 10^4$ ) in the jet self-similarity region.

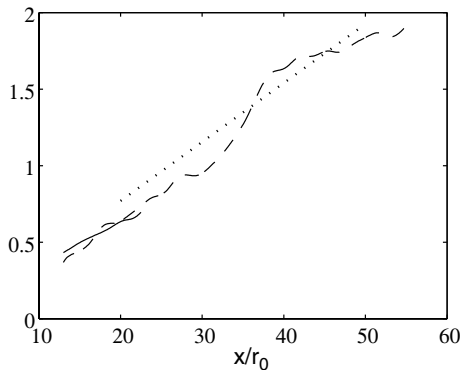


Fig. 15. Axial profile of the length scale  $L_{11}^{(1)} / r_0$  on the jet axis for: (—) LESac, (---) LESaero. (···) line  $L_{11}^{(1)} = 0.0385x$  measured by Wygnanski and Fiedler [43].

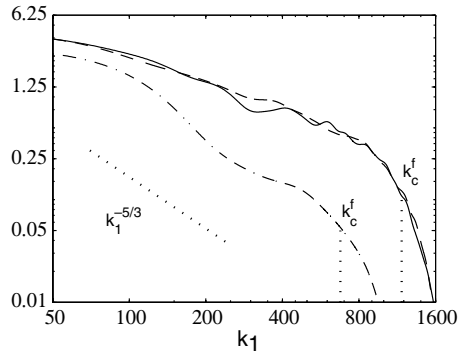


Fig. 16. One-dimensional spectrum  $E_u^{(1)}(k_1)$  of the fluctuating axial velocity  $u'$ , as a function of the axial wave number  $k_1$ , and calculated on the jet axis at  $x = 20r_0$ , for (—) LESac and for (---) LESaero, and at  $x = 50r_0$  (···) for LESaero ( $k_c^f$  are the local filtering cut-off wave numbers).

$x = 50r_0$  on the jet axis. They are obtained from the temporal spectra  $E_u(f)$ , using the Taylor hypothesis of a frozen turbulence yielding  $k_1 = 2\pi f / \langle u \rangle$  and  $E_u^{(1)}(k_1) = E_f(f) \times \langle u \rangle / (2\pi)$  where  $k_1$  is the wave number in the axial direction,  $f$  the frequency, and  $\langle u \rangle$  the mean axial velocity. The computations of

$E_u(f)$  for the simulations LESaero and LESac involve the final  $6 \times 10^4$  and  $3.5 \times 10^4$  iterations, as shown in Table 1. The signal durations  $T_{usp}$  are chosen so that  $D/(T_{usp} u_j) = 6.5 \times 10^{-4}$  and  $1.1 \times 10^{-3}$  in terms of minimal Strouhal number. They are divided, respectively, into 341 and 199 overlapping sections. The filtering cut-off wave numbers  $k_c^f$ , approximated by  $\pi/(2\Delta x)$  where  $\Delta x$  is the local mesh spacing in the axial direction, are also represented. As expected, the spectra collapse in the vicinity of  $k_c^f$ .

The two spectra from LESaero and LESac for  $x = 20r_0$  are superposed. Their shapes are basically different from the shape of the spectrum for  $x = 50r_0$ . The latter spectrum displays a decrease possibly following the  $k_1^{-5/3}$  dimensional law just before the grid cut-off wave number, but such a behaviour is not observed for the two former spectra. Therefore an inertial zone of turbulence where the energy is transferred from larger to smaller scales seems to be found for  $x = 50r_0$  but not for  $x = 20r_0$ .

To discuss this, characteristic wave numbers of the turbulence, corresponding to the axial integral scales, to the transverse Taylor scales  $\lambda_g$  and to the Kolmogorov scales  $\eta$ , are reported in Table 2 for the two points where the  $u'$ -spectra are considered. The Taylor and Kolmogorov scales are calculated using the relations of isotropic turbulence, i.e.  $\lambda_g = (15L_{11}^{(1)} v / u')^{1/2}$  and  $\eta = (L_{11}^{(1)})^{1/4} (v / u')^{3/4}$ . There is a large difference between the Taylor and the Kolmogorov wave numbers, which implies that an inertial zone is likely to be found in

Table 2

Wave numbers associated to the axial integral length scale, to the grid cut-off, to the transverse Taylor scale and to the Kolmogorov scale, for  $x = 20r_0$  and  $x = 50r_0$  on the jet axis

	$x = 20r_0$	$x = 50r_0$
$1/L_{11}^{(1)}$	160	50
$k_c$	1100	700
$1/\lambda_g$	4800	2300
$1/\eta$	200 000	110 000

the two cases. However, the grid cut-off wave numbers are not located identically with respect to the integral-scale wave numbers. For  $x = 20r_0$ , the ratio between  $k_c$  and  $1/L_{11}^{(1)}$  is about 7, whereas it is about 14 for  $x = 50r_0$ . Thus the inertial zone for  $x = 20r_0$  may not be taken into account by the grid, whereas a part of the inertial zone for  $x = 50r_0$  may be resolved.

## 5. Acoustic field

The pressure field provided directly by the LESac simulation is now investigated to determine if it agrees with that expected for a high Reynolds number, subsonic jet.

### 5.1. Sound pressure spectra

Sound pressure spectra are presented in Fig. 17. They are calculated at four locations, defined by  $(x = 29r_0, r = 11r_0)$ ,  $(x = 29r_0, r = 15r_0)$ ,  $(x = 20r_0, r = 15r_0)$  and  $(x = 11r_0, r = 15r_0)$ , by averaging over 31 points equally spaced azimuthally on half a circle. These locations are subsequently referred to by angles  $\theta$  of  $30^\circ, 40^\circ, 60^\circ$  and  $80^\circ$ , respectively. The angles are taken from the jet axis direction, with an origin chosen around the end of the potential core where the dominant sound sources are likely to be found. As shown in Table 1, the final  $3.3 \times 10^4$  iterations of the simulation are used for computing the spectra. The total time sampling  $T_{ac}$  is divided into 199 overlapping sections, and is such that  $D/(T_{ac}u_j) = 1.2 \times 10^{-3}$  in term of minimal Strouhal number.

The spectra of Fig. 17(a) appear basically different according to the observation angle. The downstream spectra for  $\theta = 30^\circ$  and  $40^\circ$  are dominated by a low-frequency component with a peak for a Strouhal number  $St \simeq 0.3$ . The sideline spectrum for  $\theta = 80^\circ$  displays a more broadband shape with a maximum observed for

$St \simeq 0.7$ . Finally, the spectrum for  $\theta = 60^\circ$  is intermediary since its shape exhibits the properties of the two former shapes with two maxima for about  $St \simeq 0.4$  and  $St \simeq 0.75$  which are however not very pronounced. The variation of the sound spectra as a function of the observation angle is in good agreement with the observations of the noise radiated by jets with high Reynolds numbers [15]. The effective Reynolds number of the computed jet therefore corresponds to the Reynolds number given by the inflow conditions. This is important to demonstrate the feasibility of computing high Reynolds number flows by LES.

Moreover, the present results support the idea proposed by Tam et al. [46] which evidenced two distinct components in jet noise from a large database of spectra for both subsonic and supersonic jets: the first component radiates more strongly in the downstream direction and could be associated with large scales/instability waves, and the second one dominates in the sideline and the upstream direction and could be attributed to the fine-scale turbulence. The first noise mechanism has recently been investigated by means of numerical simulations of low or moderate Reynolds number jets, and can be equally connected to the decay of instability waves [2] or to the periodic intrusion of vortical structures in the jet [4] at the end of the potential core. The second noise mechanism needs a sufficiently high Reynolds number to be observed, and thus can be looked into numerically only by an LES.

For a more quantitative comparison with experiments, the downstream spectrum for  $\theta \simeq 30^\circ$  is represented in Fig. 17(b) with the corresponding data of Jordan et al. [31] measured in the acoustic far-field and arbitrarily shifted in amplitude for the comparison. We can thus focus on the spectral shape, see in Section 5.3 for the discussion on the amplitude. The computed and experimental spectral shapes are in good agreement. The peaks are obtained for close Strouhal numbers of  $St \simeq 0.3$  and  $St \simeq 0.25$ , respectively. The decreases for

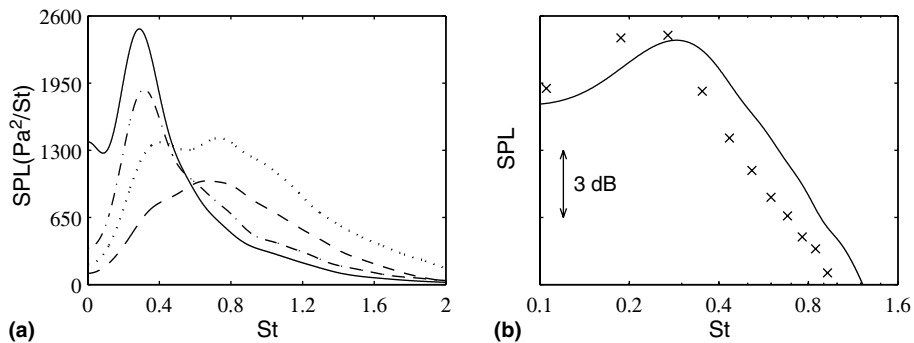


Fig. 17. (a) Sound pressure spectra, in linear scales, as a function of Strouhal number  $St = fD/u_j$  for: (—)  $x = 29r_0$  and  $r = 12r_0$ , (----)  $x = 29r_0$  and  $r = 15r_0$ , (···)  $x = 20r_0$  and  $r = 15r_0$ , (---)  $x = 11r_0$  and  $r = 15r_0$ , i.e. for angles  $\theta$  from the jet axis of about  $30^\circ, 40^\circ, 60^\circ, 80^\circ$  respectively. (b) Sound spectrum, in logarithmic scales, for  $\theta \simeq 30^\circ$ .  $\times$  measurements of Jordan et al. [31] ( $M = 0.9$ ,  $Re_D = 10^6$ , for  $30^\circ$  and  $60r_0$  from the nozzle), shifted in amplitude for the comparison of the shapes.

high Strouhal numbers are also quite similar. The computed spectrum seems however slightly more marked for high frequencies. This little discrepancy may be due to the locations of the observation points: measurements are made in far-field, typically in the cone of silence of the jet where high frequency noise is lacking because of refraction effects, whereas the computed spectrum is only obtained for  $x = 29r_0$  and  $r = 11r_0$  where fine-scale noise may not be completely negligible. The possible presence of fine-scale noise is also illustrated by the spectrum for  $\theta \simeq 40^\circ$  where the high-frequency component is clearly enhanced with respect to the spectrum for  $\theta \simeq 30^\circ$ .

In the sideline direction, the pressure spectrum has a broadband shape typical of a high Reynolds number, and it reaches a peak for Strouhal  $St \simeq 0.7$  which appears higher than the peak at  $St \simeq 0.4$  usually displayed by far-field sideline experimental spectra. This shift in frequency may partially be due to the fact that the computed spectrum is obtained only at  $x = 11r_0$  and  $r = 15r_0$ . Thus, the fine-scale noise generated in the shear layers and at the end of the potential core is preferentially observed, rather than the fine-scale noise radiated downstream. However an extrapolation of the sound waves in the far acoustic field, using for instance Kirchhoff method [47], is likely not to modify the sideline spectrum sufficiently to recover a maximum around  $St \simeq 0.4$ . We rather think that the shift towards higher Strouhal numbers with respect to measurements is a feature of the present calculation. Its origin may be found in the shear-layer transition as also discussed in Section 5.3 for the sound pressure levels. Note finally that the shape of the sideline spectrum calculated from similar LES was recently found not to depend significantly on the inflow conditions [16].

## 5.2. Azimuthal cross-correlations

The azimuthal cross-correlations of the fluctuating pressure are now presented in Fig. 18(a). They are calcu-

lated for the four observation points defined in Fig. 17(a) corresponding to  $\theta \simeq 30^\circ, 40^\circ, 60^\circ$  and  $80^\circ$ , by

$$R_{pp}(\phi) = \frac{\langle p'(\phi_0)p'(\phi_0 + \phi) \rangle}{\langle p'^2(\phi_0) \rangle^{1/2} \langle p'^2(\phi_0 + \phi) \rangle^{1/2}}$$

where  $\phi$  is the azimuthal angle, and  $\phi_0$  an arbitrary reference angle.

The correlation functions differ greatly according to the observation angle  $\theta$ , as for the sound spectra. The correlation level decreases spectacularly as  $\theta$  increases, as is found in experimental observations [48,49] on high Reynolds number, subsonic jets. For  $\theta \simeq 30^\circ$  and  $\theta \simeq 40^\circ$ , the correlation levels are very high, with for example  $R_{pp} \simeq 0.4–0.5$  for  $\phi = 180^\circ$ . For  $\theta \simeq 60^\circ$  and  $\theta \simeq 80^\circ$ , the correlation functions decrease rapidly with the azimuth, and the sound field is only correlated over a range of about  $30^\circ$ . There is a good correspondence between the changes in the spectra and in the azimuthal correlations. This supports the presence of two noise mechanisms: a first one associated to large scales within the jet generating downstream a highly correlated sound field, and a second one associated to turbulence and responsible for a more isotropic and decorrelated sound field.

Comparisons with experimental correlation functions are shown in Fig. 18(b) for  $\theta = 30^\circ$  and  $\theta = 80^\circ$ . For both angles, there is a good agreement with measurements of Maestrello [48] conducted on high subsonic jets. This validates the spatial structure of the sound field computed by LES.

## 5.3. Sound pressure levels

Contours of the overall sound pressure levels in dB are presented in Fig. 19. They illustrate the strong directivity of jet noise in the downstream direction, and also show that the inflow forcing near  $x = r_0$  has negligible effects on the radiated sound field. To compare with experiments, the  $1/d$  decay law is used to extrapolate far-field sound levels from these near-field levels. The

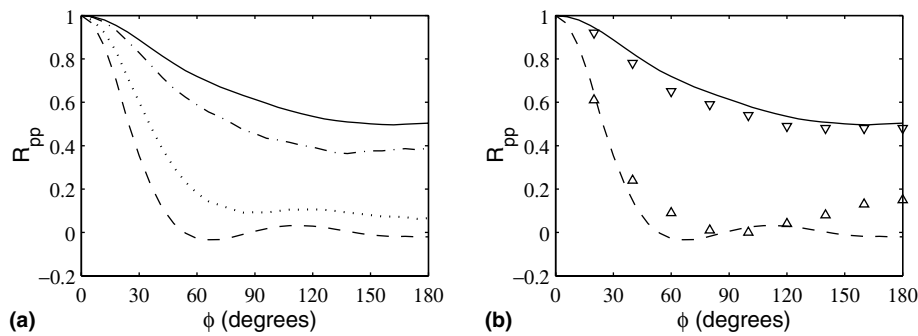


Fig. 18. (a) Azimuthal cross-correlations of the fluctuating pressure for: (—)  $\theta \simeq 30^\circ$ , (---)  $\theta \simeq 40^\circ$ , (···)  $\theta \simeq 60^\circ$ , (—·—)  $\theta \simeq 80^\circ$ . (b) Comparison with measurements: ( $\nabla$ ) Maestrello [48] ( $M = 0.85$ ,  $Re_D = 5.1 \times 10^5$ ,  $\theta \simeq 30^\circ$ ), ( $\Delta$ ) Maestrello [48,49] ( $M = 0.7$ ,  $Re_D = 4.3 \times 10^5$ ,  $\theta \simeq 90^\circ$ ).

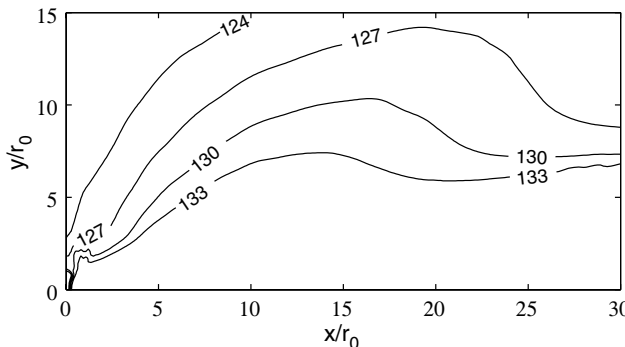


Fig. 19. Contours of the overall sound pressure levels, in dB, in the  $x-y$  plane at  $z = 0$ .

two points corresponding to radiation angles about  $30^\circ$  and  $80^\circ$  are considered to evaluate both the downstream and sideline sound pressure amplitudes.

The sound radiation at about  $30^\circ$  from the jet axis is first studied. The sound level for the point  $x = 29r_0$  and  $y = 12r_0$  (125.2 dB) is extrapolated to a distance of 60 radii from the source region assumed to be at  $x = 10r_0$  on the jet axis, at the end of the potential core [4]. The extrapolated level is 116.7 dB, which is in good agreement with measurements at  $\theta = 30^\circ$  for cold (Mollo-Christensen et al. [33]: 116.3 dB, Tanna [34]: 114.6 dB) and isothermal (Jordan et al. [31]: 115.5 dB) jets at Mach 0.9.

The sound radiation in the sideline direction is then investigated. The sound level obtained at  $x = 11r_0$  and  $y = 15r_0$  (124.1 dB) is extrapolated using the  $1/d$  decay law of acoustic waves, from a source region chosen to be at  $x = 7r_0$  on the jet axis as suggested by the snapshots of pressure fields of Fig. 6(b). This defines an angle of sound emission from the jet axis of  $\theta \approx 75^\circ$ . The sound level at 60 radii from the source region is found to be 112.3 dB, which is 4 or 5 dB higher than the corresponding experimental data at  $\theta \approx 75^\circ$  (Jordan et al. [31]: 106 dB, Mollo-Christensen et al. [33]: 108.2 dB, Tanna [34]: 108.3 dB). The origin of this discrepancy is still not clearly identified, but it is expected to be found in the shear-layer turbulence which generates an important part of the sideline noise [42]. This level overestimation may result from the turbulent transition occurring in the shear layer, which is likely to depend appreciably on the jet inflow forcing. It was indeed very recently found that removing the first four azimuthal mode from the forcing can lead to a reduction of 2 dB in the sideline noise levels [16]. However further investigations are required to overcome this amplitude problem.

## 6. Conclusion

A circular isothermal jet with a Mach number  $M = 0.9$  and a Reynolds number  $Re_D = 4 \times 10^5$  is com-

puted by large eddy simulation (LES) on two grids to investigate both the flow and the sound fields. Instead of an eddy-viscosity model, a filtering is applied explicitly to ensure the dissipation of the subgrid scales. The filtering is selective enough so that the LES results, related to the large-scale features, are not significantly affected by the choice of its application parameters.

The flow fields provided by the two simulations are very similar which shows the independence of the numerical results regarding the location of the mesh boundaries. The mean flow and turbulence properties, as well as the sound pressure field, compare favourably with experimental data on similar jets. The effective Reynolds number of the simulated jet appears also to correspond well to the high Reynolds number  $Re_D$  defined by the inflow conditions. This is particularly supported by the behaviour of the sound spectra and azimuthal correlations which vary strongly as a function of the observation angle. The present observations are also in accordance with the theory suggesting that there would be two components in jet noise: a first one associated to large scales, radiating preferentially downstream, and a second one usually associated to the fine-scale turbulence. However there is a problem with the sideline sound levels which are higher than expected and this needs to be further investigated.

The present work is thus a necessary preliminary step before using LES data to investigate noise generation mechanisms [18], but subsequent works are required to clearly understand what must be done to perform LES of jets with full confidence. For this, the database provided by the present paper can be used as a reference solution, to study for instance the effects on the jet development and on its radiated sound of the jet initial conditions [16] or those of the traditional subgrid modellings proposed in the literature [17].

## Acknowledgement

This work was supported by the EU Research programme JEAN (Jet Exhaust Aerodynamics and Noise) (Contract No. G4RD-CT-2000-00313) and by the french RRIT “Recherche Aéronautique sur le Supersonique” (Ministère de la Recherche). Computing time is supplied by the Institut du Développement et des Ressources en Informatique Scientifique (IDRIS—CNRS).

## Appendix A. A 21-point stencil selective filter

To remove grid-to-grid oscillations likely to appear in the diagonals of Cartesian grid sections, a selective filter was developed. It is fourth-order only, but its coefficients  $d_j^d$  are optimized so that the dissipation is minimized up to  $k\Delta = \pi/\sqrt{2}$ , where  $\Delta$  is the distance

Table 3

Coefficients  $d_j^d$  for the selective filter on 21 points ( $d_{-j}^d = d_j^d$ )

$d_0^d$	=	0.12254360
$d_1^d$	=	-0.11724974
$d_2^d$	=	0.10266357
$d_3^d$	=	-0.08202111
$d_4^d$	=	0.05939469
$d_5^d$	=	-0.03857436
$d_6^d$	=	0.02209702
$d_7^d$	=	-0.01086446
$d_8^d$	=	0.00436333
$d_9^d$	=	-0.00129033
$d_{10}^d$	=	0.00020959

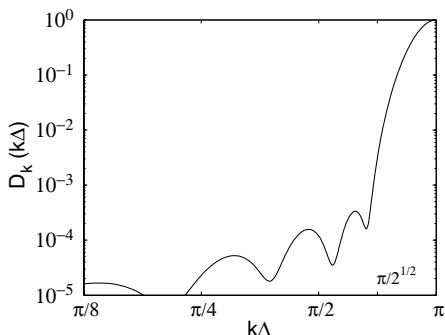


Fig. 20. Damping function, in logarithmic scales, of the 21-point stencil selective filter.

between two points located in the diagonals of a section of a uniform grid of size step  $\Delta x$  ( $\Delta = \sqrt{2}\Delta x$ ). The coefficients  $d_j^d$  of the filter are presented in Table 3 and the corresponding damping function  $D_k(k\Delta) = d_0^d + \sum_{j=1}^{10} 2d_j^d \cos(jk\Delta)$  is displayed in Fig. 20.

As for selective filters previously proposed by the authors [11], the two criteria  $D_k \leq 2.5 \times 10^{-3}$  and  $D_k \leq 2.5 \times 10^{-4}$  are used to provide  $\lambda_p/\Delta$  and  $\lambda_a/\Delta$ , i.e. the accuracy limits indicating the waves, respectively, properly and accurately resolved. The accuracy limits are found to be  $\lambda_p/\Delta = 4.02/\sqrt{2}$  and  $\lambda_a/\Delta = 4.76/\sqrt{2}$ . These values agree well with the accuracy limit of about  $\lambda/\Delta x = 4$  imposed in the Cartesian grid directions.

## References

- [1] Tam CKW. Computational aeroacoustics: issues and methods. AIAA J 1995;33:1788–96.
- [2] Freund JB. Noise sources in a low-Reynolds-number turbulent jet at Mach 0.9. J Fluid Mech 2001;438:277–305.
- [3] Morris PJ, Long LN, Scheidegger TE. Parallel computations of high speed jet noise. AIAA Paper 99-1873, 1999.
- [4] Bogey C, Bailly C, Juvé D. Noise investigation of a high subsonic, moderate Reynolds number jet using a compressible LES. Theor Comput Fluid Dynam 2003;16:273–97.
- [5] Zhao W, Frankel SH, Mongeau L. Large eddy simulations of sound radiation from subsonic turbulent jets. AIAA J 2001;39:1469–77.
- [6] Constantinescu GS, Lele SK. Large eddy simulation of a near sonic turbulent jet and its radiated noise. AIAA Paper 2001-0376, 2001.
- [7] Uzun A, Blaisdell GA, Lyrintzis AS. Recent progress towards a large eddy simulation code for jet aeroacoustics. AIAA Paper 2002-2598, 2002.
- [8] Lupoglazoff N, Biancherin A, Vuillot F, Rahier G. Comprehensive 3D unsteady simulations of subsonic and supersonic hot jet flow-fields. AIAA Papers 2002-2599 and 2002-2600, 2002.
- [9] Bogey C, Bailly C, Juvé D. Numerical simulation of the sound generated by vortex pairing in a mixing layer. AIAA J 2000;38:2210–8.
- [10] Bogey C, Bailly C. Three-dimensional non reflective boundary conditions for acoustic simulations: far-field formulation and validation test cases. Acta Acust 2002;88:463–71.
- [11] Bogey C, Bailly C. A family of low dispersive and low dissipative explicit schemes for flow and noise computations. J Comput Phys 2004;194:194–214.
- [12] Visbal MR, Rizzetta DP. Large-eddy simulation on curvilinear grids using compact differencing and filtering schemes. J Fluid Eng 2002;124:836–47.
- [13] Rizzetta DP, Visbal MR, Blaisdell GA. A time-implicit high-order compact differencing and filtering scheme for large-eddy simulation. Int J Numer Methods Fluids 2003;42:665–93.
- [14] Mathew J, Lechner R, Foysi H, Sesterhenn J, Friedrich R. An explicit filtering method for large eddy simulation of compressible flows. Phys Fluids 2003;15:2279–89.
- [15] Lush PA. Measurements of subsonic jet noise and comparison with theory. J Fluid Mech 1971;46:477–500.
- [16] Bogey C, Bailly C. Effects of inflow conditions and forcing on subsonic jet flows and noise. AIAA J 2005;43:1000–7.
- [17] Bogey C, Bailly C. Decrease of the effective Reynolds number with eddy-viscosity subgrid-scale modeling. AIAA J 2005;43:437–9.
- [18] Bogey C, Bailly C. Investigation of subsonic jet noise using LES: Mach and Reynolds number effects. AIAA Paper 2004-3023, 2004.
- [19] Vreman B, Geurts B, Kuerten H. Subgrid-modelling in LES of compressible flow. Appl Sci Res 1995;54:191–203.
- [20] Lesieur M, Métais O. New trends in large-eddy simulations of turbulence. Annu Rev Fluid Mech 1996;28:45–82.
- [21] Meneveau C, Katz J. Scale-invariance and turbulence models for large-eddy simulation. Annu Rev Fluid Mech 2000;32:1–32.
- [22] Sagaut P. Large eddy simulation for incompressible flows. Berlin: Springer; 2001.
- [23] Domaradzki JA, Adams NA. Direct modelling of subgrid scales of turbulence in large eddy simulation. J Turbulence 2002;3.
- [24] Smagorinsky JS. General circulation experiments with the primitive equations: I. The basic experiment. Mon Weath Rev 1963;91:99–163.
- [25] Domaradzki JA, Yee PP. The subgrid-scale estimation model for high Reynolds number turbulence. Phys Fluids 2000;12:193–6.
- [26] Boris JP, Grinstein FF, Oran ES, Kolbe RL. New insights into large eddy simulation. Fluid Dyn Res 1992;10:199–228.
- [27] Grinstein FF, Fureby C. Recent progress on MILES for high Reynolds number flows. J Fluids Eng 2002;124:848–61.
- [28] Garnier E, Mossi M, Sagaut P, Comte P, Deville M. On the use of shock-capturing schemes for large-eddy simulation. J Comput Phys 1999;153:273–311.
- [29] Lau JC, Morris PJ, Fisher MJ. Measurements in subsonic and supersonic free jets using a laser velocimeter. J Fluid Mech 1979;93:1–27.
- [30] Simonich JC, Narayanan S, Barber TJ, Nishimura M. Aeroacoustic characterization, noise reduction, and dimensional scaling effects of high subsonic jets. AIAA J 2001;39:2062–9.
- [31] Jordan P, Gervais Y, Valière J-C, Foulon H. Final results from single point measurements. Project deliverable D3.4, JEAN—EU 5th Framework Programme, G4RD-CT2000-00313, 2002.

- [32] Arakeri VH, Krothapalli A, Siddavaram V, Alkislar MB, Lourenco L. On the use of microjets to suppress turbulence in a Mach 0.9 axisymmetric jet. *J Fluid Mech* 2003;490:75–98.
- [33] Mollo-Christensen E, Kolpin MA, Martucelli JR. Experiments on jet flows and jet noise far-field spectra and directivity patterns. *J Fluid Mech* 1964;18:285–301.
- [34] Tanna HK. An experimental study of jet noise. Part I: Turbulent mixing noise. *J Sound Vib* 1977;50:405–28.
- [35] Zaman KBM. Far-field noise of a subsonic jet under controlled excitation. *J Fluid Mech* 1985;152:83–111.
- [36] Juvé D, Sunyach M, Comte-Bellot G. Intermittency of the noise emission in subsonic cold jets. *J Sound Vib* 1980;71:319–32.
- [37] Rudy DH, Strikwerda JC. A nonreflecting outflow boundary conditions for subsonic Navier–Stokes calculations. *J Comput Phys* 1980;36:55–70.
- [38] Poinsot TJ, Lele SK. Boundary conditions for direct simulations of compressible viscous flows. *J Comput Phys* 1992;101:104–29.
- [39] Stoltz S, Adams NA, Kleiser L. An approximate deconvolution model for large-eddy simulation with application to incompressible wall-bounded flows. *Phys Fluids* 2001;13:997–1015.
- [40] Ricou FP, Spalding DB. Measurements of entrainment by axisymmetrical turbulent jets. *J Fluid Mech* 1961;11:21–32.
- [41] Islam MT, Ali MAT. Mean velocity and static pressure distributions of a circular jet. *AIAA J* 1997;35:196–7.
- [42] Zaman KBM. Flow field and near and far sound field of a subsonic jet. *J Sound Vib* 1986;106:1–16.
- [43] Wygnanski I, Fiedler H. Some measurements in the self-preserving jet. *J Fluid Mech* 1969;38:577–612.
- [44] Panchapakesan NR, Lumley JL. Turbulence measurements in axisymmetric jets of air and helium. Part I. Air jet. *J Fluid Mech* 1993;246:197–223.
- [45] Hussein HJ, Capp SP, George WK. Velocity measurements in a high-Reynolds-number, momentum-conserving, axisymmetric, turbulent jet. *J Fluid Mech* 1994;258:31–75.
- [46] Tam CKW, Golebiowski M, Seiner JM. On the two components of turbulent mixing noise from supersonic jets. *AIAA Paper* 96-1716, 1996.
- [47] Gloerfelt X, Bailly C, Juvé D. Direct computation of the noise radiated by a subsonic cavity flow and application of integral methods. *J Sound Vib* 2003;266:119–46.
- [48] Maestrello L. Two points correlations of sound pressure in the far field of a jet: Experiment. NASA-TMX-72835, 1976.
- [49] Juvé D, Sunyach M. Structure azimutale du champ acoustique lointain d'un jet subsonique. *CR Acad Sci Paris* 1978;287(B): 187–190 (in french).